AAAS
Energy Material Advances
Volume 2021, Article ID 2585274, 9 pages
https://doi.org/10.34133/2021/2585274

Energy Material Advances
A SCIENCE PARTNER JOURNAL

Research Article

Lattice Doping of Lanthanide Ions in $Cs_2AgInCl_6$ Nanocrystals Enabling Tunable Photoluminescence

Ying Liu,[1] Maxim S. Molokeev,[2,3,4] and Zhiguo Xia[1,5]

[1]*The Beijing Municipal Key Laboratory of New Energy Materials and Technologies, School of Materials Science and Engineering, University of Science and Technology, Beijing, China*
[2]*Laboratory of Crystal Physics, Kirensky Institute of Physics, Federal Research Center KSC SB RASs, Russia*
[3]*Department of Engineering Physics and Radioelectronics, Siberian Federal University, Russia*
[4]*Department of Physics, Far Eastern State Transport University, Russia*
[5]*The State Key Laboratory of Luminescent Materials and Devices, Guangdong Provincial Key Laboratory of Fiber Laser Materials and Applied Techniques, School of Materials Science and Engineering, South China University of Technology, China*

Correspondence should be addressed to Zhiguo Xia; xiazg@scut.edu.cn

Received 11 December 2020; Accepted 22 January 2021; Published 24 February 2021

Lead-free halide double perovskite $Cs_2AgInCl_6$ has become the research hotspot in the optoelectronic fields. It is a challenge to utilize the lattice doping by different lanthanide ions with rich and unique photoluminescence (PL) emissions for emerging photonic applications. Here, we successfully incorporated Dy^{3+}, Sm^{3+}, and Tb^{3+} ions into $Cs_2AgInCl_6$ nanocrystals (NCs) by the hot-injection method, bringing diverse PL emissions of yellowish, orange, and green light in $Cs_2AgInCl_6$:Ln^{3+} ($Ln^{3+} = Dy^{3+}$, Sm^{3+}, Tb^{3+}). Moreover, benefiting from the energy transfer process, Sm^{3+} and Tb^{3+} ion-codoped $Cs_2AgInCl_6$ NCs achieved tunable emission from green to yellow orange and a fluorescent pattern from the as-prepared NC-hexane inks by spray coating was made to show its potential application in fluorescent signs and anticounterfeiting technology. This work indicates that lanthanide ions could endow $Cs_2AgInCl_6$ NCs the unique and tunable PL properties and stimulate the development of lead-free halide perovskite materials for new optoelectronic applications.

1. Introduction

Lead halide perovskites have become the legend in the history of material science for emerging optoelectronic application due to their tunable emissions, high photoluminescence quantum yield (PLQY), easy solution processability, and so on [1–4]. Nevertheless, considering their lead toxicity and low stability, it is urgent to seek environmentally friendly semiconductor materials in this database. At this time, lead-free halide perovskites were discovered with lower toxicity and higher stability and have attracted great interests [5–9]. There are many choices for the replacement of Pb^{2+} by other benign metal ions, including the incorporation of isovalent Sn^{2+} ions [10] and substitution of trivalent Bi^{3+} or Sb^{3+} ions forming the similar composition as $Cs_3Bi_2Cl_9$ [11–13]. However, those materials are either limited by stability challenges [14] or with lower electronic mobility because of the lower symmetry nonperovskite structure [15]. One different way to address the challenge is to replace two Pb^{2+} ions with one monovalent cation (B^+ ions) and one trivalent cation (B^{3+} ions), forming the three-dimensional (3D) double perovskite structure [16]. The possible combinations of various cations make the diversity of lead-free double perovskites and make them the most promising alternative for optoelectronic applications [17].

Lead-free halide double perovskites with the general formula $A_2B^+B^{3+}X_6$ ($A = Cs^+$; $B^+ = Cu^+, Ag^+, Na^+$; $B^{3+} = Bi^{3+}, Sb^{3+}, In^{3+}$; $X = Cl^-, Br^-, I^-$) crystallize in a cubic unit cell with the space group $Fm\bar{3}m$ [18]. Among them, Cs_2AgBiX_6 and $Cs_2NaBiCl_6$ possess an indirect band gap leading to a low absorption coefficient and a weak photoluminescence (PL) emission [19, 20]. In contrast, $Cs_2AgInCl_6$, inheriting the relatively good performance of the lead halide perovskites mainly attributed to the nature of direct band gap, has drawn increasing attention after the discovery by Giustino et al. [21] and Zhou et al. [22] and the milestone work as white light

emitters by Luo et al. [7]. $Cs_2AgInCl_6$ is reported to have a long carrier lifetime, easy solution processability, and a direct band gap with a parity-forbidden transition that results in a low PLQY (<0.1%), and a full story on research history of $Cs_2AgInCl_6$ has been summarized recently for the details [23]. The poor PLQY has been improved by different doping and alloying strategies [7, 24–26]. Nevertheless, the PL of $Cs_2AgInCl_6$ nanocrystals (NCs) contains a broadband spectral profile owing to the origin of self-trapped excitons (STEs) [27]. Therefore, to explore doped $Cs_2AgInCl_6$ NCs with improved PLQY and tunable emission is a main challenge. Generally, lanthanide (Ln^{3+}) ions would be the most suitable dopants for their rich and unique PL emissions in the visible to near-infrared range [28, 29], which could be utilized to achieve tunable luminescence and increased PLQY [30]. Moreover, the successful incorporation of rare earth ions for the lead-based halide perovskites [31, 32] and the structural similarity between lead-based and lead-free perovskites (both with the six octahedral coordination number) have provided the reference and opportunities to conduct the further lanthanide doping study on $Cs_2AgInCl_6$ NCs [33–35].

In this work, different lanthanide ions ($Ln^{3+} = Dy^{3+}, Sm^{3+}, Tb^{3+}$) were successfully incorporated into $Cs_2AgInCl_6$ perovskite NCs through the hot-injection method developed by our group [26]. Dy^{3+}, Tb^{3+}, and Sm^{3+} ions were verified to occupy the In^{3+} site in the $Cs_2AgInCl_6$ lattice. The introduction of these rare earth ions endowed $Cs_2AgInCl_6$ with diverse PL emissions in the visible region. Benefiting from the energy transfer process, Sm^{3+}/Tb^{3+}-codoped $Cs_2AgInCl_6$ NCs achieved tunable emission from green to yellow orange and a fluorescent pattern from the as-prepared NC-hexane inks by spray coating was made to show its potential application in fluorescent signs and anticounterfeiting technology. This work expands the PL emissions of lead-free perovskite NCs through lanthanide ion doping, making them more competitive and will promote a wider regulation for their optical properties and novel photonic applications in energy-related materials.

2. Materials and Methods

2.1. Materials. Cesium carbonate (Cs_2CO_3, 99.9%), indium chloride ($InCl_3$, 99.99%), dysprosium chloride hexahydrate ($DyCl_3 \bullet 6H_2O$, 99.9%), terbium (III) nitrate pentahydrate ($Tb(NO_3)_3 \cdot 5H_2O$, 99.9%), samarium (III) chloride ($SmCl_3$, 99.9%), octadecene (ODE, >90%), oleylamine (OLA, 80-90%), oleic acid (OA, analytical pure), hexane (C_6H_{14}, ≥98%), and ethyl acetate ($C_4H_8O_2$, analytical pure) were purchased from Aldrich. Silver nitrate ($AgNO_3$, analytical pure) and hydrochloric acid (HCl, analytical pure) were purchased from Beijing Chemical Works, China. All the chemicals were used directly without further purification.

2.2. Synthesis of Cs-Oleate. 0.814 g of Cs_2CO_3 was loaded into a mixture of ODE (10 mL) and OA (2.5 mL), heated to 120°C and degassed by alternating vacuum and N_2 for 1 h. Then, the reaction mixture was filled with N_2 and heated to 150°C.

2.3. Synthesis of Ln^{3+} (Ln = Dy, Tb, Sm)-Doped $Cs_2AgInCl_6$ NCs. Adequate amount of lanthanide raw materials ($DyCl_3 \cdot 6H_2O$: 0.036 mmol, $Tb(NO_3)_3 \cdot 5H_2O$: 0.108 mmol, $SmCl_3$: 0.072 mmol) was added into the mixture of $AgNO_3$ (0.36 mmol), $InCl_3$ (0.36 mmol), ODE (14 mL), OA (1 mL), OLA (1 mL), and HCl (0.28 mL). The reaction solution was heated to 120°C and degassed by alternating vacuum and N_2 for 1 h. Then, the mixture was heated to 260°C under N_2. The as-prepared hot (150°C) Cs-oleate solution (0.8 mL) was quickly injected into the solution. After ~20 s, the system was transferred to an ice-water bath. The crude sample was centrifuged at 8000 rpm for 4 min, discarding the supernatant. Next, the precipitate was dispersed in hexane and centrifuged again at 5000 rpm for 4 min, leaving the supernatant. The final NCs were precipitated with ethyl acetate by centrifugating for 4 min at 10000 rpm. For Sm^{3+}- and Tb^{3+}-codoped samples, different doping concentrations (5 mol%, 10 mol%, 20 mol%, and 40 mol%) of Sm^{3+} were added at the fixed concentration of Tb^{3+} (0.108 mmol).

2.4. Characterization. X-ray diffraction (XRD) measurements were carried out on an Aeris X-ray diffractometer (PANalytical Corporation, Netherlands) equipped with a 50000 mW Cu Kα radiation after dropping concentrated nanocrystal hexane solutions on the silicon substrates. Transmission electron microscopy (TEM) images and energy-dispersive X-ray spectroscopy (EDS) analysis were acquired on a JEM-2010 microscope transmission electron microscope at the voltage of 120 kV equipped with an energy-dispersive detector, for which the samples were prepared by dropping dilute nanocrystal hexane solutions on the ultrathin carbon film-mounted Cu grids. Steady-state photoluminescence (PL) spectra, photoluminescence excitation (PLE) spectra, and PL decay spectra were recorded using a FLS920 fluorescence spectrometer (Edinburgh Instruments Ltd., U.K.) which is equipped with the Xe900 lamp, nF920 flash lamp, and the PMT detector. UV-visible absorption spectra were collected using a Hitachi UH4150 UV-vis-near IR spectrophotometer. Elemental contents were determined by the inductively coupled plasma mass spectroscopy (ICP-MS) after treating samples with wet digestion method. X-ray photoelectron spectroscopy (XPS) was carried out on the ESCALAB 250Xi instrument (Thermo Fisher). The PL quantum yields were obtained on the Hamamatsu absolute PL quantum yield spectrometer C11347 Quantaurus_QY.

3. Results

3.1. Structural Analysis of Ln^{3+} (Ln = Dy, Tb, Sm)-Doped $Cs_2AgInCl_6$ NCs. Ln^{3+} ion (Dy^{3+}, Sm^{3+}, Tb^{3+})-doped $Cs_2AgInCl_6$ NCs were synthesized by a hot-injection method at 260°C as illustrated in Figure S1. The X-ray diffraction (XRD) patterns showed that all the doped samples possessed pure phase (Figure 1(a)) and all peaks of them were indexed by cubic cell ($Fm\ \bar{3}\ m$) with the parameters close to $Cs_2AgInCl_6$ (Figures 1(b)–1(e)) [21]. This indicated that the incorporation of Ln^{3+} ions into $Cs_2AgInCl_6$ does not change the phase structure. To verify the location of Ln^{3+} ions, Rietveld refinement was performed using

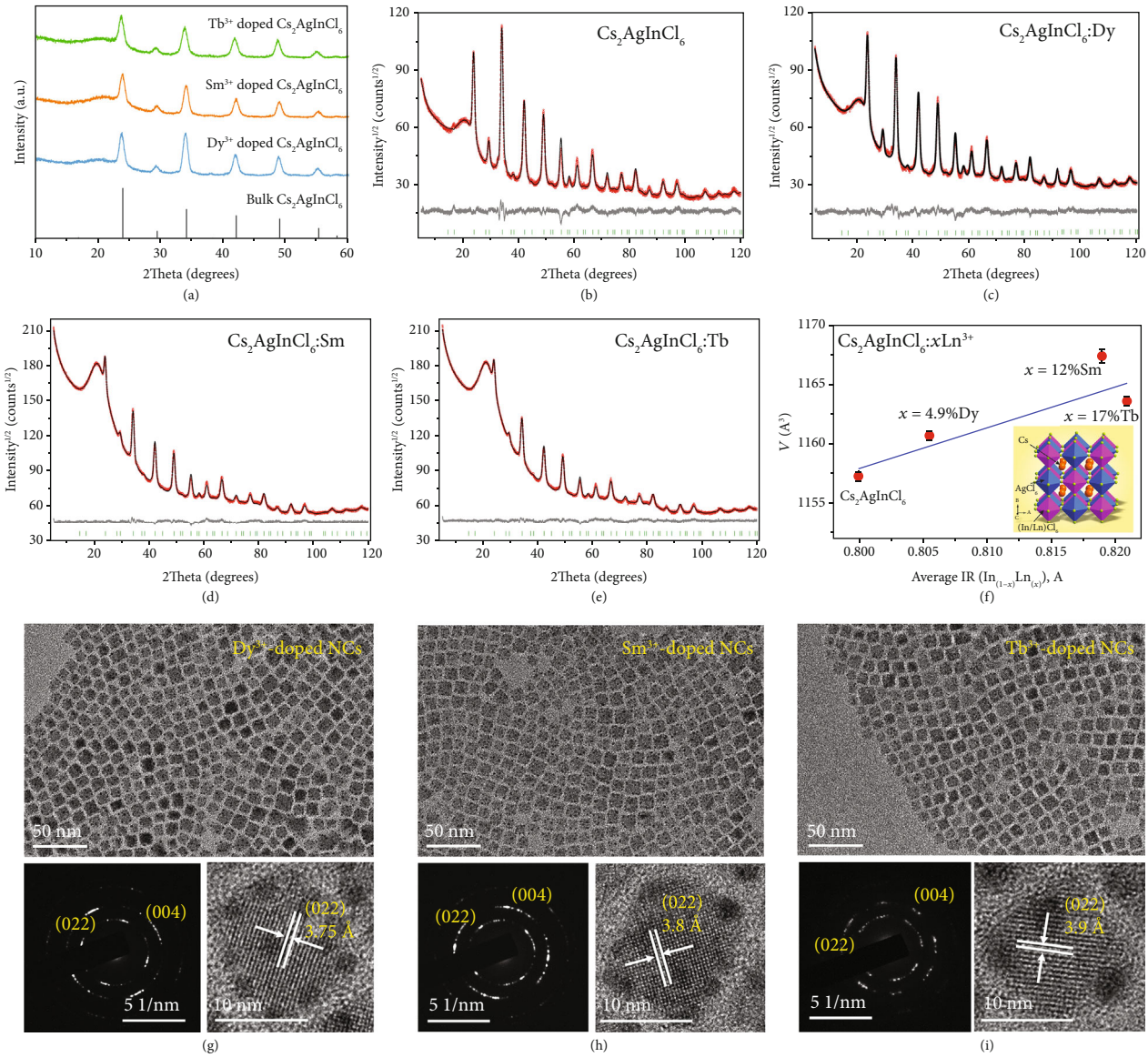

FIGURE 1: Structural characterization of Ln^{3+} (Ln = Dy, Sm, Tb)-doped $Cs_2AgInCl_6$ NCs. (a) XRD patterns and (b–e) Rietveld refinements of XRD patterns for undoped and Ln^{3+}-doped $Cs_2AgInCl_6$ NCs. (f) The cell volume of $Cs_2AgIn_{1-x}Cl_6$:xLn versus dopant concentration (x = 0, 5%Dy, 12%Sm, 17%Tb). (g–i) TEM images (up), selected area electron diffraction (SAED) patterns (left bottom), and high-resolution TEM images (right bottom) for Dy^{3+}-doped, Sm^{3+}-doped, and Tb^{3+}-doped $Cs_2AgInCl_6$ NCs.

TOPAS 4.2 software. The refinements were stable and showed low R factors (Table S1). The coordinates of atoms and main bond lengths are given in Tables S2 and S3, respectively. It was found that cell volumes of compounds increased with Ln^{3+} ions doped (Figure 1(f)). All the ion radii of Ln^{3+} dopants with 6-coordination (IR $(Dy^{3+}) = 0.912$ Å; IR $(Sm^{3+}) = 0.958$ Å; IR $(Tb^{3+}) = 0.923$ Å) were smaller than those of Ag^+ (IR $(Ag^+, CN = 6) = 1.15$ Å) and Cs^+ (IR $(Cs^+, CN = 8) = 1.74$ Å) ions, inconsistent with the increasing trend of cell volumes. Therefore, it cannot be explained by the model of $Ln^{3+} \leftrightarrow Cs^+$ or $Ln^{3+} \leftrightarrow Ag^+$ ion replacements. On the other hand, the ion radii of Ln^{3+} dopants were larger than those of In^{3+} ion (IR $(In^{3+}, CN = 6) = 0.8$ Å), which was in a good agreement with the increasing trend of cell volumes. Hence, Ln^{3+} ions are proposed to occupy the sites of In^{3+} ions, as shown in the inset of Figure 1(f). The actual doping concentrations detected by inductively coupled plasma (ICP) measurement were 5% for Dy^{3+} ions, 12% for Sm^{3+} ions, and 17% for Tb^{3+} ions. To see the micromorphology of the NCs, transmission electron microscopy (TEM) images of Ln^{3+} ion-doped NCs were exhibited in Figures 1(g)–1(i). As revealed by TEM, all the Ln^{3+} ion (Dy^{3+}, Sm^{3+}, Tb^{3+})-doped $Cs_2AgInCl_6$ NCs demonstrated the similar uniform cubic shape with the mean size of 9.68, 10.26, and 10.46 nm, respectively (Figure S2). The selected area electron diffraction (SAED) signals for the three Ln^{3+} ion-doped NCs all showed the presence of (022) and (004) planes of cubic phase, further verifying the formation of the

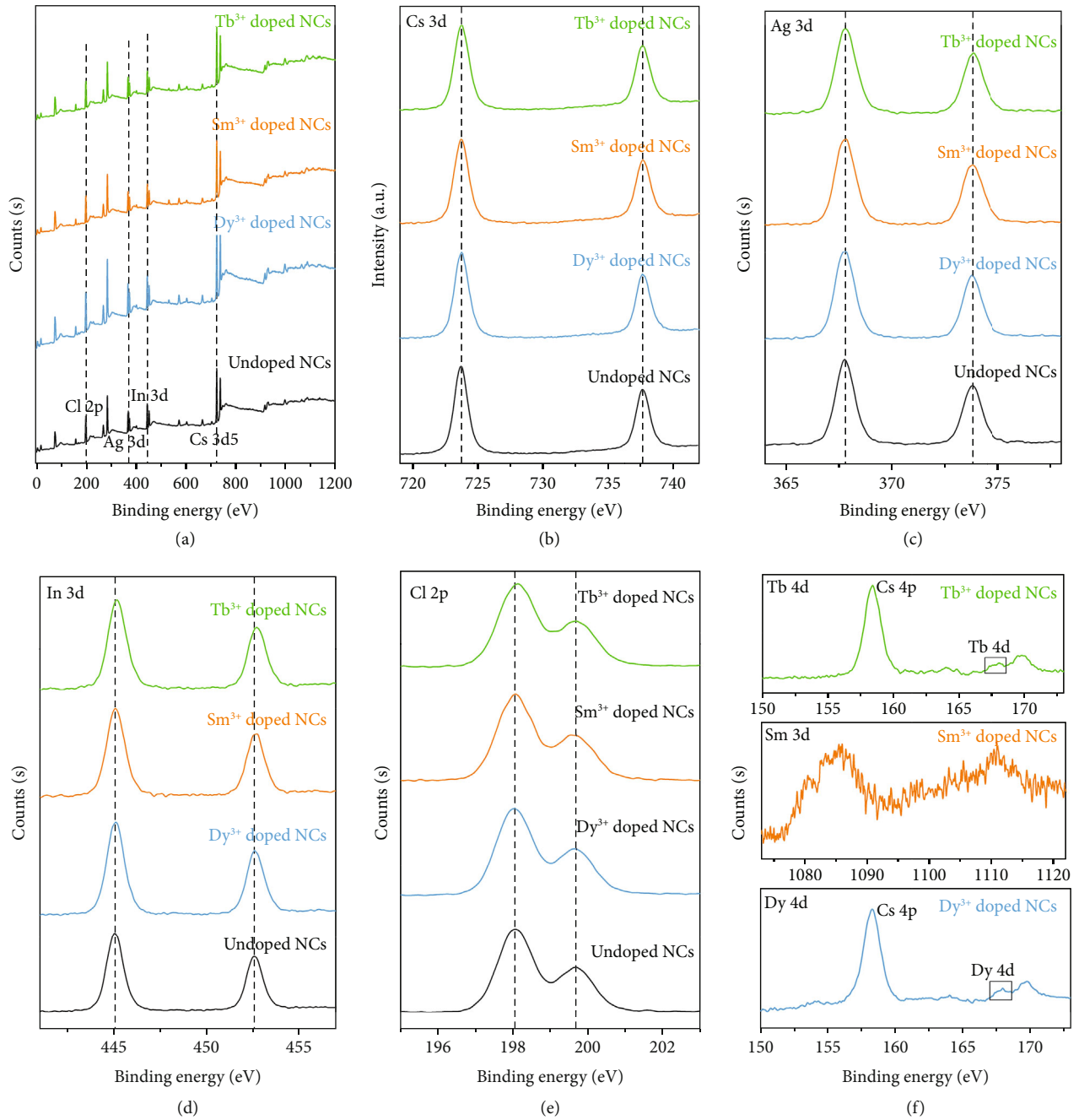

FIGURE 2: Elemental analysis of Ln^{3+} (Ln = Dy, Sm, Tb)-doped $Cs_2AgInCl_6$ NCs. (a) Survey XPS spectra for the undoped and Dy^{3+}-doped, Sm^{3+}-doped, and Tb^{3+}-doped $Cs_2AgInCl_6$ NCs. (b–e) High-resolution XPS spectra for Cs 3d, Ag 3d, In 3d, and Cl 2p, respectively. (f) High-resolution XPS spectra for the Dy^{3+} 4d, Sm^{3+} 3d, and Tb^{3+} 4d for Dy^{3+}-doped, Sm^{3+}-doped, and Tb^{3+}-doped $Cs_2AgInCl_6$ NCs, respectively.

same perovskite structure as $Cs_2AgInCl_6$. The existence of doped Dy^{3+}, Sm^{3+}, and Tb^{3+} ions in $Cs_2AgInCl_6$ NCs could be confirmed by energy-dispersive X-ray (EDS) analysis and corresponding elemental mapping images (Figure S3). The high-resolution TEM (HRTEM) images in Figures 1(g)–1(i) revealed that the incorporation of Ln^{3+} ions did not induce the formation of crystal defects and the clear lattice fringes with the increasing lattice constants of 3.75 Å, 3.8 Å, and 3.9 Å for Dy^{3+}, Sm^{3+}, and Tb^{3+} ions doped, respectively, corresponded to the (022) interplane distance (3.7 Å) of $Cs_2AgInCl_6$. The increased interplane distances further indicated the successful incorporation of Dy^{3+}, Sm^{3+}, and Tb^{3+} ions.

To further characterize the chemical compositions of Ln^{3+}-doped $Cs_2AgInCl_6$ NCs, X-ray photoelectron spectroscopy (XPS) measurements were carried out. As shown in the XPS survey spectra (Figure 2(a)), the signals of Cs, Ag, In, and Cl were clearly observed in every sample. The respective high-resolution XPS spectra are present in Figures 2(b)–2(e). As for the Cs 3d and In 3d XPS spectra, there was a slight shift to higher binding energy as Dy^{3+}, Sm^{3+}, and Tb^{3+} ions were introduced, attributed to changed chemical

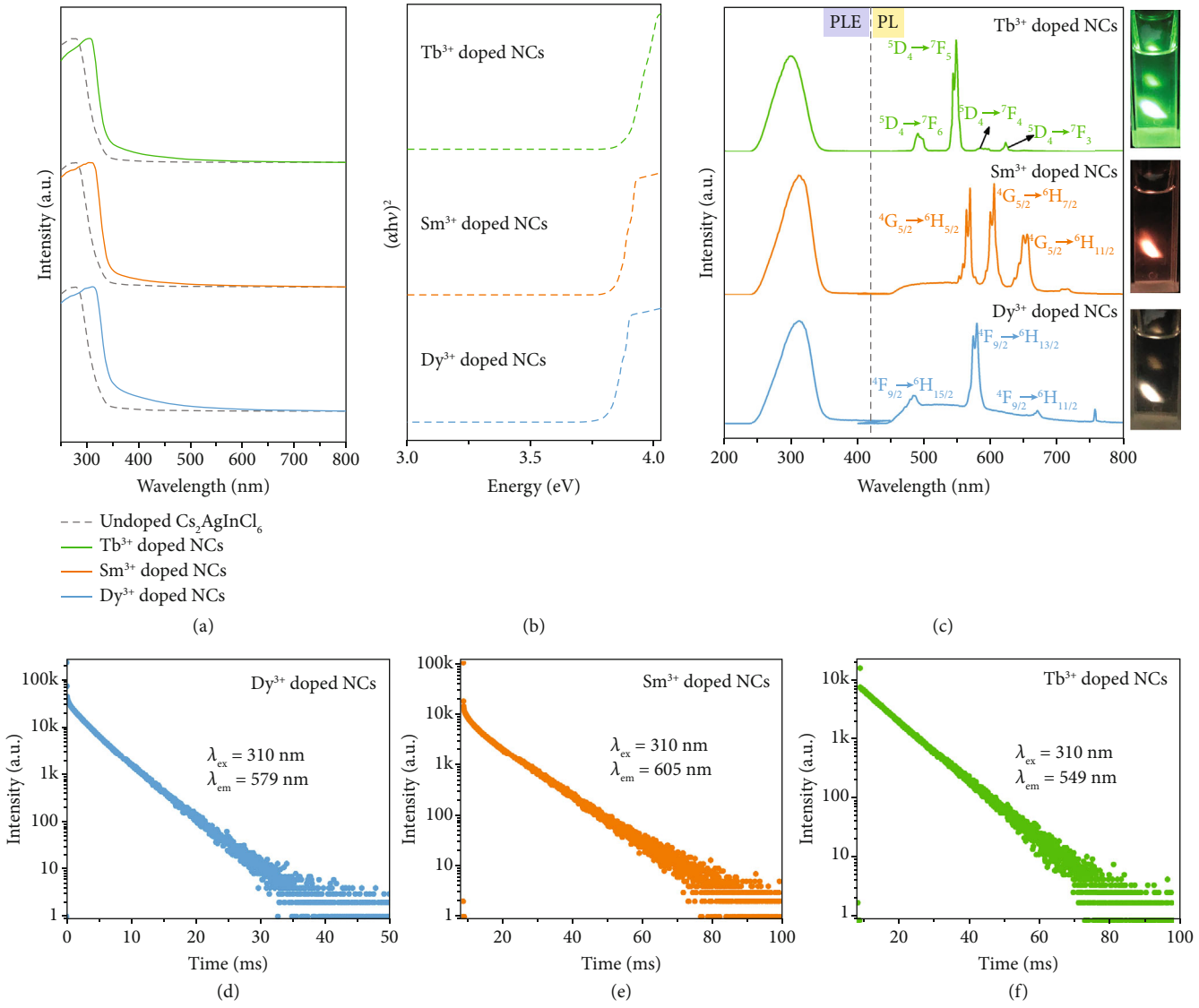

FIGURE 3: Optical properties of Ln^{3+} (Ln = Dy, Sm, Tb)-doped $Cs_2AgInCl_6$ NCs. (a) Absorption spectra and (b) corresponding T_{auc} plots of Dy^{3+}-doped, Sm^{3+}-doped, Tb^{3+}-doped, and undoped $Cs_2AgInCl_6$ NCs. (c) PLE (monitored at 579 nm for Dy^{3+}-doped NCs, at 605 nm for Sm^{3+}-doped NCs, and at 549 nm for Dy^{3+}-doped NCs) and PL spectra excited by 310 nm. The insets of (c) show the photographs of the corresponding doped samples under 310 nm UV irradiation. (d–f) PL decay spectra for different NCs doped with Dy^{3+}, Sm^{3+}, and Tb^{3+} ions.

environments of In^{3+} and Cs^+ in terms of the samples doped with Ln^{3+} ions, while for the Ag 3d the spectra showed almost the same peak position for the undoped and three Ln^{3+} ion-doped $Cs_2AgInCl_6$ NCs. Moreover, the relatively weak signals peaked at 167.9 eV, 1085 and 1110 eV, and 167.3 eV are observed in Figure 2(f) corresponding to the binding energy of Dy 4d, Sm 3d, and Tb 4d, respectively [36, 37]. The weak signals may be due to the small amount of lanthanide ions on the surface. Combined with the XRD analysis, those results further indicated that Ln^{3+} ions were successfully doped into the perovskite host lattice and located in the site of In^{3+} to alter the local coordination structures.

3.2. Optical Properties of Ln^{3+} (Ln = Dy, Tb, Sm)-Doped $Cs_2AgInCl_6$ NCs. The optical features of the as-prepared Ln^{3+}-doped $Cs_2AgInCl_6$ NCs were investigated (Figure 3). All samples showed a strong absorption starting at around 350 nm and peaked at ~310 nm (Figure 3(a)). Additionally, it is clear that there was a red shift of the excitonic absorption peak with Ln^{3+} ion doping, which could be ascribed to the size increase of NCs. The optical band gaps 3.83 eV, 3.85 eV, and 3.88 eV for Dy^{3+}-doped, Sm^{3+}-doped, and Tb^{3+}-doped NCs were quantified from the T_{auc} plots of $(\alpha h\nu)^2$, which were calculated from the corresponding absorption spectra (Figure 3(b)). The decrease in optical band gaps compared with ~4 eV of undoped $Cs_2AgInCl_6$ NCs [26] could be attributed from the lattice expansion of doped NCs [38]. Doped with different lanthanide ions, the as-synthesized NCs present variable emission (Figure 3(c)). Under 310 nm excitation, Dy^{3+}-doped, Sm^{3+}-doped, and

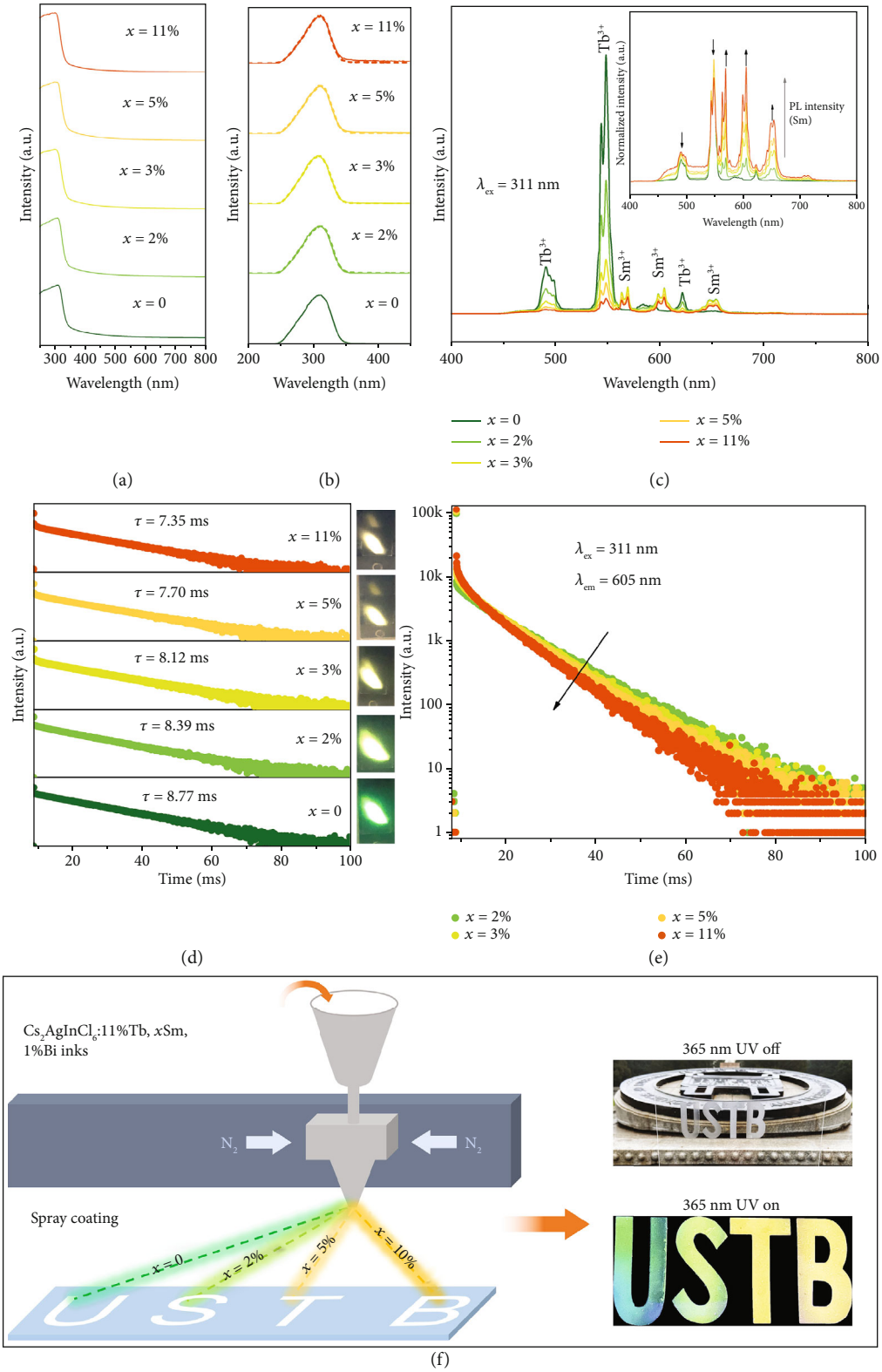

FIGURE 4: Optical properties and application of Sm^{3+}- and Tb^{3+}-codoped $Cs_2AgInCl_6$ NCs. (a) Absorption spectra, (b) excitation spectra (solid line: monitored at 548 nm; dash line: monitored at 605 nm), and (c) PL spectra excited by 311 nm of $Cs_2AgIn_{(0.89-x)}Cl_6$:0.11Tb NCs dependent with different Sm doping concentrations x ($x = 0$, 2%, 3%, 5%, and 11%). The inset of (c): corresponding normalized PL spectra. (d) PL decay spectra monitored at 548 nm emission and 311 nm excitation with the photographs of the corresponding codoped samples under 311 nm UV irradiation. (e) PL decay spectra monitored at 605 nm emission and 311 nm excitation. (f) Scheme of spray coating using Bi-doped $Cs_2AgIn_{(0.89-x)}Cl_6$:0.11Tb,xSm NCs as different inks.

Tb^{3+}-doped NCs exhibited the characteristic emissions of Dy^{3+}, Sm^{3+}, and Tb^{3+} ions with the PLQY values of 2.8%, 3.1%, and 9.2%, respectively, and the irradiated NC solutions upon UV light were demonstrated in the insets of Figure 3(c). The sharp peaks therein were corresponding to the intrinsic transitions of $^4F_{5/2}$-^6H_J (J = 15/2, 13/2, 11/2) for Dy^{3+} ions, $^4G_{5/2}$-^6H_J (J = 2/5, 2/7, 2/9, 2/11) for Sm^{3+} ions, and $^5D_4$-^7F_J (J = 6, 5, 4, 3) for Tb^{3+} ions, respectively. All the PLE spectra monitored at the respective peak positions of three Ln^{3+} ions were almost the same, which matches closely with the PLE spectrum of $Cs_2AgInCl_6$ NC host seen in the previous work by Alivisatos et al. [39] and in our group [26]. That indicated that the emissions of Ln^{3+}-doped NCs were most likely to originate from an efficient energy transfer from $Cs_2AgInCl_6$ NC host to the energy levels of Dy^{3+}, Sm^{3+}, and Tb^{3+} ions [40], as illustrated in Figure S4. The PL decay curves of the three lanthanide ion-doped samples were measured (Figure 3(d), Table S4) and fitted by

$$\tau_{ave} = \sum_i A_i \tau_i. \quad (1)$$

The calculated lifetimes for Dy^{3+}-doped, Sm^{3+}-doped, and Tb^{3+}-doped NCs were 3.29 ms, 8.1 ms, and 8.45 ms, respectively, consistent with the recent reports on these lanthanide ion-doped luminescent materials [41, 42].

3.3. Tunable Luminescence of Sm^{3+}- and Tb^{3+}-Codoped $Cs_2AgInCl_6$ NCs. Energy transfer between the codoped lanthanide ions in one system is a general strategy to achieve tunable luminescence. We design the controlled experiments by doping Tb^{3+} ions in $Cs_2AgInCl_6$ NCs with different amounts of Sm^{3+} ions (Figure 4). The general amount of Sm^{3+} and Tb^{3+} dopants was determined by ICP-MS measurement. As shown in Figure 4(a), all samples showed a strong absorption starting at ~350 nm and peaked at around 310 nm. The PLE spectra of $Cs_2AgIn_{(0.89-x)}Cl_6$:0.11Tb,xSm NCs were almost the same when monitored at 548 and 605 nm, further suggesting that the emissions of Sm^{3+} and Tb^{3+} ions were also derived from the efficient energy transfer from $Cs_2AgInCl_6$ NC host to lanthanide ions (Figure 4(b)). Figure 4(c) reveals the PL emission for different amounts of Sm^{3+}-doped $Cs_2AgIn_{(0.89-x)}Cl_6$:0.11Tb NCs under the excitation of 311 nm. The PLQYs were measured to be 5.9%, 5.5%, and 5.0%, respectively, corresponding to the Sm^{3+} concentrations of 3%, 5%, and 11%. With the increase in the amount of Sm^{3+} dopants, the PL intensity of Tb^{3+} emission decreases and the PL intensity of Sm^{3+} emission increases first and then decreases. Thus, the emission colors could be tuned from green to yellow orange. The weakening of Sm^{3+} emission was attributed to the concentration quenching effect. To reveal the variation trend of PL intensity more directly, the PL spectra were normalized as shown in the inset of Figure 4(c). It was found that the normalized peak intensity of Tb^{3+} ions decreased and the luminescent intensity of Sm^{3+} ions increased gradually. Those results indicated the possible occurrence of $Tb^{3+} \rightarrow Sm^{3+}$ energy transfer in $Cs_2AgInCl_6$ NCs. Moreover, the decay curves of 11%Tb^{3+}/$x$$Sm^{3+}$ (x = 0, 2%, 3%, 5%, and 11%)-codoped $Cs_2AgInCl_6$ NCs by recording Tb^{3+} 548 nm emission at 311 nm excitation are shown in Figure 4(d) to investigate the energy transfer process from Tb^{3+} to Sm^{3+} ions. The lifetimes calculated from Figure 4(d) and Table S5 for $x$$Sm^{3+}$ (x = 0, 2%, 3%, 5%, and 11%)-doped $Cs_2AgIn_{(0.89-x)}Tb_{0.11}Cl_6$ NCs were 8.77, 8.39, 8.12, 7.70, and 7.35 ms, respectively, which showed that with the increase in the concentration of Sm^{3+} ion dopants, the fluorescence lifetime of Tb^{3+} ion emission decreased gradually. That evidence further confirmed the existence of the energy transfer channel from Tb^{3+} to Sm^{3+} ions in $Cs_2AgInCl_6$ NCs. Sm^{3+} emission decays monitored at 605 nm emission and 311 nm excitation were also revealed in Figure 4(e). It was found that with the increase in the doping amount of Sm^{3+} ions, the fluorescence decays became faster, attributed to the concentration quenching effect of Sm^{3+} ion dopants. In addition, we used Bi^{3+}-doped $Cs_2AgIn_{(0.89-x)}Tb_{0.11}Cl_6$:$x$Sm NCs to make fluorescent signs by spray coating. Bi^{3+} ion incorporation could adjust the excitation to 365 nm for wider application from our previous work [34]. The scheme of spray coating process is demonstrated in Figure 4(f), in which different NC-hexane solutions were atomized into very small droplets from the nozzle with the high-pressurized nitrogen gas. Then, the droplets deposited onto the PMMA substrate, forming the desired uniform, stable, and high-resolution patterns. The fluorescence patterns with tunable emissions shown in the right side of Figure 4(f) could respond to the 365 nm UV excitation signal, revealing the potential application of lanthanide ion-doped $Cs_2AgInCl_6$ NCs in the field of anticounterfeiting technology and fluorescent signs.

4. Discussion

In conclusion, we demonstrated the successful lattice doping of various lanthanide ions, including Dy^{3+}, Tb^{3+}, and Sm^{3+}, into lead-free perovskite $Cs_2AgInCl_6$ NCs through the hot-injection method. It was confirmed by structural refinements that Dy^{3+}, Tb^{3+}, and Sm^{3+} ions occupied the site of In^{3+} ions, and the TEM images and XPS analysis further verified this result. The introduction of Ln^{3+} doping endowed $Cs_2AgInCl_6$ with diverse PL emissions in the visible region. Benefiting from the energy transfer process, Sm^{3+}/Tb^{3+}-codoped $Cs_2AgInCl_6$ NCs achieved tunable emission from green to yellow orange and a fluorescent pattern from the as-prepared NC-hexane inks by spray coating was made to show its application in fluorescent signs and anticounterfeiting technology. This work extends the study on lanthanide ion doping into lead-free halide perovskite $Cs_2AgInCl_6$ NCs and further enables a wider regulation for their optical properties and applications in energy-related materials.

Data Availability

All data needed to evaluate the conclusions in the paper are present in the paper and/or the Supplementary Materials. Additional data related to this paper may be requested from the authors.

Conflicts of Interest

The authors declare that there is no conflict of interest regarding the publication of this article.

Authors' Contributions

Z.G.X. initiated and guided the research. Y.L. and Z.G.X. discussed and wrote the manuscript. Y.L. performed the experiments. M.S.M. performed Rietveld refinement of the power X-ray diffraction results.

Acknowledgments

This work was supported by the National Natural Science Foundation of China (grant numbers 51961145101 and 51972118), the Fundamental Research Funds for the Central Universities (grant number FRFTP-18-002C1), the Guangzhou Science & Technology Project (202007020005), and the Local Innovative and Research Teams Project of Guangdong Pearl River Talents Program (grant number 2017BT01X137). This work was also funded by RFBR according to the research project no. 19-52-80003.

Supplementary Materials

Figures S1–S4 and Tables S1–S5 show the synthesis scheme, size distribution of NCs, TEM-EDS spectra and mapping images, energy-level diagram, structural refinement data, and calculated PL lifetimes. *(Supplementary Materials)*

References

[1] K. M. Boopathi, B. Martín-García, A. Ray et al., "Permanent lattice compression of lead-halide perovskite for persistently enhanced optoelectronic properties," *ACS Energy Letters*, vol. 5, no. 2, pp. 642–649, 2020.

[2] Q. A. Akkerman, G. Raino, M. V. Kovalenko, and L. Manna, "Genesis, challenges and opportunities for colloidal lead halide perovskite nanocrystals," *Nature Materials*, vol. 17, no. 5, pp. 394–405, 2018.

[3] Q. Zhou, Z. Bai, W. G. Lu, Y. Wang, B. Zou, and H. Zhong, "In situ fabrication of halide perovskite nanocrystal-embedded polymer composite films with enhanced photoluminescence for display backlights," *Advanced Materials*, vol. 28, no. 41, pp. 9163–9168, 2016.

[4] X. Li, Y. Wang, H. Sun, and H. Zeng, "Amino-mediated anchoring perovskite quantum dots for stable and low-threshold random lasing," *Advanced Materials*, vol. 29, no. 36, article 1701185, 2017.

[5] J. Huang, T. Lei, M. Siron et al., "Lead-free cesium europium halide perovskite nanocrystals," *Nano Letters*, vol. 20, no. 5, pp. 3734–3739, 2020.

[6] Z. Xiao, Z. Song, and Y. Yan, "From lead halide perovskites to lead-free metal halide perovskites and perovskite derivatives," *Advanced Materials*, vol. 31, article e1803792, 2018.

[7] J. Luo, X. Wang, S. Li et al., "Efficient and stable emission of warm-white light from lead-free halide double perovskites," *Nature*, vol. 563, no. 7732, pp. 541–545, 2018.

[8] S. Bhaumik, S. Ray, and S. K. Batabyal, "Recent advances of lead-free metal halide perovskite single crystals and nanocrystals: synthesis, crystal structure, optical properties, and their diverse applications," *Materials Today Chemistry*, vol. 18, article 100363, 2020.

[9] X. Zhu, L. Bian, H. Fu et al., "Broadband perovskite quantum dot spectrometer beyond human visual resolution," *Light: Science & Applications*, vol. 9, no. 1, p. 73, 2020.

[10] J. Islam and A. Hossain, "Semiconducting to metallic transition with outstanding optoelectronic properties of $CsSnCl_3$ perovskite under pressure," *Scientific Reports*, vol. 10, no. 1, p. 14391, 2020.

[11] J. Pal, S. Manna, A. Mondal, S. Das, K. V. Adarsh, and A. Nag, "Colloidal synthesis and photophysics of $M_3Sb_2I_9$(M = Cs and Rb) nanocrystals: lead-free perovskites," *Angewandte Chemie, International Edition*, vol. 56, no. 45, pp. 14187–14191, 2017.

[12] M. Leng, Y. Yang, K. Zeng et al., "All-inorganic bismuth-based perovskite quantum dots with bright blue photoluminescence and excellent stability," *Advanced Functional Materials*, vol. 28, no. 1, article 1704446, 2018.

[13] A. Pradhan, S. C. Sahoo, A. K. Sahu, and S. L. Samal, "Effect of Bi substitution on $Cs_3Sb_2Cl_9$: structural phase transition and band gap engineering," *Crystal Growth & Design*, vol. 20, no. 5, pp. 3386–3395, 2020.

[14] Z. Wu, Q. Zhang, B. Li et al., "Stabilizing the $CsSnCl_3$ perovskite lattice by B-site substitution for enhanced light emission," *Chemistry of Materials*, vol. 31, no. 14, pp. 4999–5004, 2019.

[15] F. Jiang, D. Yang, Y. Jiang et al., "Chlorine-incorporation-induced formation of the layered phase for antimony-based lead-free perovskite solar cells," *Journal of the American Chemical Society*, vol. 140, no. 3, pp. 1019–1027, 2018.

[16] T. Zhang, Z. Cai, and S. Chen, "Chemical trends in the thermodynamic stability and band gaps of 980 halide double perovskites: a high-throughput first-principles study," *ACS Applied Materials & Interfaces*, vol. 12, no. 18, pp. 20680–20690, 2020.

[17] W. Zhu, W. Ma, Y. Su et al., "Low-dose real-time X-ray imaging with nontoxic double perovskite scintillators," *Light: Science & Applications*, vol. 9, no. 1, p. 112, 2020.

[18] Y. Wu, X. Li, and H. B. Zeng, "Lead-free halide double perovskites: structure, luminescence, and applications," *Small Structures*, no. article 2000071, 2020.

[19] Y. Bekenstein, J. C. Dahl, J. Huang et al., "The making and breaking of lead-free double perovskite nanocrystals of cesium silver–bismuth halide compositions," *Nano Letters*, vol. 18, no. 6, pp. 3502–3508, 2018.

[20] M. M. Yao, L. Wang, J. S. Yao et al., "Improving lead-free double perovskite $Cs_2NaBiCl_6$ nanocrystal optical properties via ion doping," *Advanced Optical Materials*, vol. 8, no. 8, article 1901919, 2020.

[21] G. Volonakis, A. A. Haghighirad, R. L. Milot et al., "$Cs_2InAgCl_6$: a new lead-free halide double perovskite with direct band gap," *Journal of Physical Chemistry Letters*, vol. 8, no. 4, pp. 772–778, 2017.

[22] J. Zhou, Z. Xia, M. S. Molokeev et al., "Composition design, optical gap and stability investigations of lead-free halide double perovskite $Cs_2AgInCl_6$," *Journal of Materials Chemistry A*, vol. 5, no. 29, pp. 15031–15037, 2017.

[23] Z. Xia, Y. Liu, A. Nag, and L. Manna, "Lead-free double perovskite $Cs_2AgInCl_6$," *Angewandte Chemie, International Edition*, 2020.

[24] W. Wu, W. Y. Cong, C. Guan et al., "Investigation of the Mn dopant-enhanced photoluminescence performance of lead-

free $Cs_2AgInCl_6$ double perovskite crystals," *Physical Chemistry Chemical Physics*, vol. 22, no. 4, pp. 1815–1819, 2020.

[25] F. Locardi, E. Sartori, J. Buha et al., "Emissive Bi-doped double perovskite $Cs_2Ag_{1-x}Na_xInCl_6$ nanocrystals," *ACS Energy Letters*, vol. 4, no. 8, pp. 1976–1982, 2019.

[26] Y. Liu, Y. Jing, J. Zhao, Q. Liu, and Z. Xia, "Design optimization of lead-free perovskite $Cs_2AgInCl_6$:Bi nanocrystals with 11.4% photoluminescence quantum yield," *Chemistry of Materials*, vol. 31, no. 9, pp. 3333–3339, 2019.

[27] P. Han, X. Zhang, X. Mao et al., "Size effect of lead-free halide double perovskite on luminescence property," *Science China Chemistry*, vol. 62, no. 10, pp. 1405–1413, 2019.

[28] W. J. Mir, T. Sheikh, H. Arfin, Z. Xia, and A. Nag, "Lanthanide doping in metal halide perovskite nanocrystals: spectral shifting, quantum cutting and optoelectronic applications," *NPG Asia Materials*, vol. 12, no. 1, p. 9, 2020.

[29] M. Zhao, Q. Zhang, and Z. Xia, "Narrow-band emitters in LED backlights for liquid-crystal displays," *Materials Today*, vol. 40, pp. 246–265, 2020.

[30] F. Schmitz, K. Guo, J. Horn et al., "Lanthanide-induced photoluminescence in lead-free $Cs_2AgBiBr_6$ bulk perovskite: insights from optical and theoretical investigations," *Journal of Physical Chemistry Letters*, vol. 11, no. 20, pp. 8893–8900, 2020.

[31] Y. Xie, B. Peng, I. Bravic et al., "Highly efficient blue-emitting $CsPbBr_3$ perovskite nanocrystals through neodymium doping," *Advancement of Science*, vol. 7, no. 20, article 2001698, 2020.

[32] N. Ding, W. Xu, D. Zhou et al., "Extremely efficient quantum-cutting Cr^{3+}, Ce^{3+}, Yb^{3+} tridoped perovskite quantum dots for highly enhancing the ultraviolet response of Silicon photodetectors with external quantum efficiency exceeding 70%," *Nano Energy*, vol. 78, p. 105278, 2020.

[33] Z. Zeng, B. Huang, X. Wang et al., "Multimodal luminescent $Yb^{3+}/Er^{3+}/Bi^{3+}$-doped perovskite single crystals for X-ray detection and anti-counterfeiting," *Advanced Materials*, vol. 32, no. 43, article e2004506, 2020.

[34] Y. Liu, X. Rong, M. Li, M. S. Molokeev, J. Zhao, and Z. Xia, "Incorporating rare-earth terbium(III) ions into $Cs_2AgInCl_6$:Bi nanocrystals toward tunable photoluminescence," *Angewandte Chemie, International Edition*, vol. 59, no. 28, pp. 11634–11640, 2020.

[35] H. Arfin, J. Kaur, T. Sheikh, S. Chakraborty, and A. Nag, "Bi^{3+}-$Er^{3+}$and Bi^{3+}-Yb^{3+} codoped $Cs_2AgInCl_6$ double perovskite near-infrared emitters," *Angewandte Chemie, International Edition*, vol. 59, no. 28, pp. 11307–11311, 2020.

[36] D. D. Sarma and C. N. R. Rao, "XPES studies of oxides of second- and third-row transition metals including rare earths," *Journal of Electron Spectroscopy and Related Phenomena*, vol. 20, no. 1, pp. 25–45, 1980.

[37] Y. Uwamino, T. Ishizuka, and H. Yamatera, "X-ray photoelectron spectroscopy of rare-earth compounds," *Journal of Electron Spectroscopy and Related Phenomena*, vol. 34, no. 1, pp. 67–78, 1984.

[38] R. Begum, M. R. Parida, A. L. Abdelhady et al., "Engineering interfacial charge transfer in $CsPbBr_3$ perovskite nanocrystals by heterovalent doping," *Journal of the American Chemical Society*, vol. 139, no. 2, pp. 731–737, 2017.

[39] J. C. Dahl, W. T. Osowiecki, Y. Cai et al., "Probing the stability and band gaps of $Cs_2AgInCl_6$ and $Cs_2AgSbCl_6$ lead-free double perovskite nanocrystals," *Chemistry of Materials*, vol. 31, no. 9, pp. 3134–3143, 2019.

[40] G. Pan, X. Bai, D. Yang et al., "Doping lanthanide into perovskite nanocrystals: highly improved and expanded optical properties," *Nano Letters*, vol. 17, no. 12, pp. 8005–8011, 2017.

[41] Y.-C. Li, Y.-H. Chang, Y.-F. Lin, Y.-S. Chang, and Y.-J. Lin, "Synthesis and luminescent properties of Ln^{3+} (Eu^{3+}, Sm^{3+}, Dy^{3+})-doped lanthanum aluminum germanate $LaAlGe_2O_7$ phosphors," *Journal of Alloys and Compounds*, vol. 439, no. 1-2, pp. 367–375, 2007.

[42] M. Chen, Z. Xia, and Q. Liu, "Ethylenediamine-assisted hydrothermal synthesis of $NaCaSiO_3OH$: controlled morphology, mechanism, and luminescence properties by doping Eu^{3+}/Tb^{3+}," *Inorganic Chemistry*, vol. 55, no. 21, pp. 11316–11322, 2016.